Available online at www.sciencedirect.com

ScienceDirect

Proceedings of the Combustion Institute 39 (2023) 4155–4164

Proceedings of the Combustion Institute

www.elsevier.com/locate/proci

Downward flame spread over PMMA spheres

David Morrisset [a,*], Rory M. Hadden [a], Angus Law [a], Jose L. Torero [b]

[a] School of Engineering, The University of Edinburgh, UK
[b] Department of Civil, Environmental & Geomatic Engineering, University College London, UK

Received 5 January 2022; accepted 11 July 2022
Available online 9 November 2022

Abstract

Experiments were conducted to measure downward flame spread over PMMA spheres, and an underpinning theoretical basis was developed to explain the relevant mechanisms governing flame spread over spherical geometries. Flame spread over a sphere was classified into two distinct regimes, that being spread over the upper and lower hemispheres. Experiments were conducted using cast PMMA spheres 40 and 50 mm in diameter. Samples were ignited at the top of the sphere and the progression of the flame front was determined using video analysis. The time resolved flame spread rate was found to increase nearly linearly in time while the flame spread across the upper hemisphere of the sample (at rates ranging from approximately 2.0–3.5 mm/min). Flame spread on the lower hemisphere was observed to accelerate nonlinearly reaching instantaneous flame spread rates greater than 15 mm/min. The flame spread rates were found to be unsteady (i.e., continuously increasing) throughout each experiment. A Stokes flow solution was found to adequately characterize the opposed flame spread rate over the upper hemisphere with respect to the induced buoyant flow. Flame spread rates in the lower hemisphere were found to be controlled by a combination of increasing velocity of the ambient flow and increased heat transfer through the interior of the solid. Flame spread rates for each diameter tested were normalized and presented as a function of the relative angle of inclination at the flame front, θ. Thus, the two regimes of flame spread identified in this work are largely independent across sphere size for the diameters used in this study. The study of flame spread over spheres provides a unique condition to observe the transition from spread dictated by a well-defined flow condition to one in which heat transfer effects through the solid become increasingly significant.

Keywords: Flame spread; Opposed flow; Downward spread; Sphere; Buoyant Flow

1. Introduction

Flame spread over solid fuels has been a topic of research for decades. Both an understanding of material characteristics and the influence of geometrical factors are required to adequately describe flame spread over a solid. Characteristics of flame spread behavior are fundamentally linked to the flow conditions at the flame front; flame spread regimes have been traditionally separated into *opposed flow* and *concurrent* flame spread based on the direction of ambient oxidizer flow. Descriptions of

* Corresponding author.
E-mail address: d.morrisset@ed.ac.uk (D. Morrisset).

https://doi.org/10.1016/j.proci.2022.07.220

opposed flow or opposed current flame spread can be readily found in literature [1–7] and serve as a foundation in much of the current understanding of flame spread mechanics. Many studies have been conducted focusing on flame spread over flat, rectangular geometries, which has since formed the basis of the current understanding of flame spread. Characterization of flame spread over other geometries is, however, limited.

Past studies have investigated opposed flame spread over cylindrical fuels, focusing primarily on microgravity applications [8,9]. Limited research has been dedicated to observing flame spread over a spherical surface [10,11] – the only studies, to the knowledge of the authors, again focus primarily on microgravity applications. Recent work has also investigated flame spread over other irregular geometries and surfaces with curvature [12,13]; there remains the need for a fundamental connection for such geometries to traditional flame spread theory.

The orientation relative to the direction of gravity continuously changes as the flame front progresses along the surface of the sphere. Previous studies have quantified the influence of sample orientation on rates of opposed flame spread [14,15] for rectangular geometries. Fernandez-Pello and Williams linked the variation in flame spread rate due to orientation to the change in the relative gravity vector and its subsequent effect on the shape of the flame sheet [15]. The continuous change in relative orientation as the flame spreads around a sphere suggests the potential for unsteady flame spread behavior around a sphere. However, the effects observed for previous studies on flat plates are linked to the resulting flame shape and do not address the influence of orientation on the leading edge of the flame. Lavid and Berlad explicitly describe the effects of buoyancy throughout a boundary layer flame and found that buoyancy effects are minor at the leading edge (i.e., Grashoff number $\sim$0) [16]. Thus, the orientation effects previously identified for flat plates are not relevant to spherical geometries as the effects at the leading edge dominate the flame spread process opposed to the flame shape; this dependence on the leading edge is demonstrated by the results of this study.

A spherical geometry provides an idealized configuration for the study of flame spread that is free from the complications of edge effects and a scenario in which a transient flame spread process can be studied. Observing downward spread over a sphere also presents a unique heat transfer condition in which the area ahead of the flame front continuously changes over the length of the sphere. This provides a condition in which heat transfer through the interior of the solid becomes increasingly significant as the flame spreads. The study of a sphere, therefore, provides an opportunity to gain insight into flame spread mechanics not captured in studying flat plates alone. To explore this, downward opposed flame spread over spheres in quiescent conditions is studied and the observed flame spread is linked to a fundamental theory relevant to this geometry.

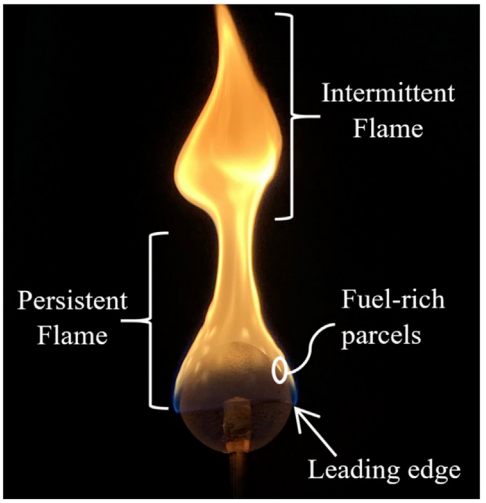

Fig. 1. An image of a 40 diameter mm PMMA sphere ignited from above to observe downward flame spread.

2. Background

Fig. 1 illustrates a burning sphere of cast PMMA which has been ignited at the top to observe opposed flame spread down the length of the sphere. The leading edge progresses down the sphere as heat is transferred to unpyrolyzed material ahead of the flame. The flame formed above the sphere exhibits both a persistent region and an intermittent region. As illustrated in Fig. 1, the leading edge is located within the persistent region. The persistent region (in particular the leading edge) can be described as laminar given the instability of the intermittent flame is sufficiently far from the leading edge. Additional time resolved images of flame spread around the sphere can be found in the appendix.

Fig. 2 illustrates the relevant length scales that characterize flame spread down the sphere. Once ignited at the top, the flame progresses along the arc length, l, as the flame front moves down the sphere's surface. Thus, l indicates the flame front position and dl/dt represents the flame spread rate, v_f, relative to the surface (i.e., relative to the arc length). The distance spanning the flame front position to the central axis of the sphere is denoted here as the flame line radius, f_l. The progression of the flame front down the sphere creates a continuous circumference around the sphere surface that can be characterized by the flame line radius and effectively describes the evolution of the leading edge.

If the flame front position is continuously measured (e.g., using video analysis), then the time re-

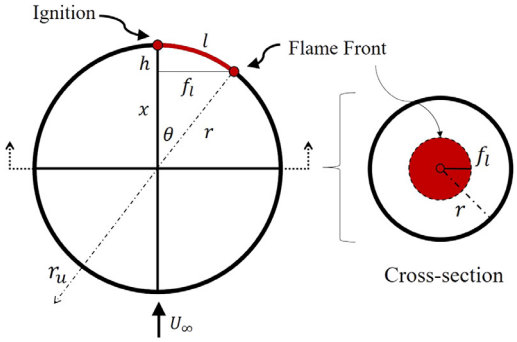

Fig. 2. A schematic representation of the relevant length scales for flame spread over a solid sphere. The cross-section cut out is presented at a reduced scale.

solved flame front position can be used to calculate the flame spread rate along the arc length. Through conventional processing techniques, video data can be used to determine the position, h, of the flame front with respect to the uppermost point. Once the position can be established, simple geometric relationships can be used to determine the angle (θ) through which the arc length can be calculated (i.e., $l = r\theta$).

While the magnitude of the arc length continuously increases over the entire sphere, f_l increases over the upper hemisphere of the fuel, but will decrease as the leading edge continues to the lower hemisphere. The transient behavior of f_l results in a varying cross-sectional area at the flame front, as indicated in Fig. 2. Thus, the flame front transfers heat to an increasingly larger area as the flame spreads over the upper hemisphere. The opposite is true for the lower hemisphere as the flame transfers heat to a continuously decreasing area at the surface.

Analytical models for describing opposed flow flame spread often characterize the flame spread rate as a function of the ambient velocity, U_∞ [2,6,7]. Fernandez-Pello previously demonstrated that if the preheated distance in front of the progressing flame, δ, is assumed to be proportional to the boundary layer thickness of the resulting flow, then the flame spread rate can be modelled as proportional to the square root of the ambient flow [6]. Thus, the flame spread rate, v_f, can be described by Eq. (1).

$$v_f = c\sqrt{\frac{U_\infty}{x}}\frac{(k\rho c_p)_g(T_f - T_P)^2}{(k\rho c_p)_s(T_P - T_o)^2} \tag{1}$$

Where c is a scaling constant, U_∞/x, is the ambient flow velocity divided by a characteristic length scale above the surface, $k\rho c_p$ is the thermal inertia (of the gas, g, and solid, s), T_f is the flame temperature, T_P is the pyrolysis temperature of the solid, and T_o is the ambient temperature. The rightmost term in Eq. (1) (i.e., everything outside the square root) can be effectively assumed constant for a sufficiently high Damköhler number [6]. Other analytical models can be employed to characterize flame spread as a function of additional flow characteristics (e.g., "stretch rate" [17]). The formulation of Eq. (1) should, however, adequately describe the relevant physics for the case of naturally buoyant flow far from blow-off conditions. Eq. (1) can then be modified further to explicitly describe the flame spread around a sphere.

Once ignited, the hot products of combustion induce a buoyant flow around the sphere. The resulting flame both entrains air from the sides and induces flow around the sphere from below. Flow around spheres has been well characterized in fluid mechanics literature (e.g., [18–20]). Analytical solutions have been established to describe the flow field as the flow passes around the sphere; for low Reynolds number flows, Eq. (2) can be used to describe the change in flow as a function of the orientation, θ, around the sphere employing a Stokes flow solution.

$$u_* = \frac{u_\theta}{U_\infty} = \sin\theta\left(1 - \frac{3R}{4r_u} - \frac{R^3}{4r_u^3}\right) \tag{2}$$

Where θ is the relative angle at the flame front, R is the outer radius of the sphere, r_u is the radial position off the surface used to characterize the flow, U_∞ is the ambient flow velocity below the sphere (see Fig. 2), and u_θ is the specific flow at any location around the sphere. A characteristic value of r_u was taken to be a 2 mm distance from the surface (i.e., $R + 2$ mm). This value was chosen to be greater than the standoff distance observed in previous flame spread experiments but within the boundary layer near the leading edge [21].

Eq. (2) illustrates that the specific flow at any given point around a sphere is dictated by $\sin\theta$ (i.e., u_θ will increase approaching the equator of the sphere, then decrease from the equator to the top). The variability of the flow around the sphere will in turn change the flow conditions at the flame front for any position along the sphere. Such variability in the flow conditions also suggest that the flame spread rate is transient as the flame spreads down the arclength (i.e., $v_f \propto \sqrt{u_\theta}$). Thus, u_θ can be used to describe the specific flow around the sphere and can therefore be incorporated into Eq. (1) to express v_f around the sphere. The ambient flow, U_∞, can be characterized as $\sqrt{gD}$ [4,5] – where g is the gravitational constant, and D is the diameter of the sphere. Thereby combining Eq. (1) and Eq. (2) with the assumed characterization of U_∞, the flame spread rate can be defined for a spherical geometry using Eq. (3).

$$v_f = c\sqrt{\frac{\sqrt{gD}\sin\theta\left(1 - \frac{3R}{4r_u} - \frac{R^3}{4r_u^3}\right)}{x}}\frac{(k\rho c_p)_g(T_f - T_P)^2}{(k\rho c_p)_s(T_P - T_o)^2} \tag{3}$$

Eq. (3) provides an analytical solution adapted to spherical geometries that relate instantaneous flame spread rates around the sphere to a given value of θ. The use of Eq. (3) is limited to scenarios in which the functionality of the Stokes flow solution (i.e., Eq. (2)) holds for the flow around the sphere. The functional significance of Eq. (3) lies in the proportionality of the flame spread rate, the specific flow velocity, and θ (e.g., $v_f \propto \sqrt{u_\theta} \propto \sqrt{\sin\theta}$); these proportionalities can then be used to describe the experimental results presented in this work.

3. Experimental methods

The experiments in this study were conducted using clear cast polymethyl methacrylate (PMMA) spheres with diameters of 40 and 50 mm. Measurements were made with a video camera positioned along the centerline of the sphere (to obtain an image as per Fig. 2). Samples were supported by a 1.5 mm diameter steel rod embedded 10 mm into the base of the sphere. Each sample was supported to allow at least 250 mm of space beneath the sphere, allowing for ample air entrainment. Spheres were ignited by contact with a nichrome hot wire (~65 W for 90 s); ignition was initiated at the top of the sphere as indicated in Fig. 1. Preliminary experiments were conducted in an effort to minimize the duration of hot wire contact needed for the experiments. The results from these experiments indicated that contact with the hot wire for short durations (e.g., less than 60 s) did not consistently sustain a flame while a 90 second exposure duration did. Trials were conducted in triplicate ($n = 3$) for the 40 mm diameter spheres, and duplicate ($n = 2$) for the 50 mm diameter spheres.

Videos were recorded with a digital camera (4K video at 25 frames/second) and were processed using Matlab to determine the progression of the flame front as a function of time. A script identified the RGB intensity of a given frame and then processed the luminance intensity of each pixel to give the flame position. The approach was developed to track the flame front by isolating the blue pixel intensity (i.e. the color of the leading edge of the flame front). Once the position of the leading edge was known, this could be differentiated with respect to time to produce the time resolved flame spread rate.

The burning of cast PMMA is characteristic of distinct bubbling and discrete losses of mass that can be observed as the pyrolysis gasses react in the flow around the sphere. The stochastic effects of bubbling and the release of finite fuel parcels are ignored in analyzing the flame spread rate; however, high frame rate video (1000 frames/s) was captured to allow the tracking of these distinct fuel parcels. This footage provided an approximate characterization of the flow surrounding the sphere – without the need of intrusive measurement techniques. Image processing for the high speed images were limited to a region of approximately 10 mm above the flame front to obtain a characteristic flow velocity at the flame front. The motion tracking was averaged over 300 frames to capture an average flow behavior at four distinct locations over the sphere surface. While the analysis is limited by a high degree of uncertainty in the precise flow rate, the high speed footage provides a qualitative description of the varying flow conditions at the leading edge as the flame spread around the sphere.

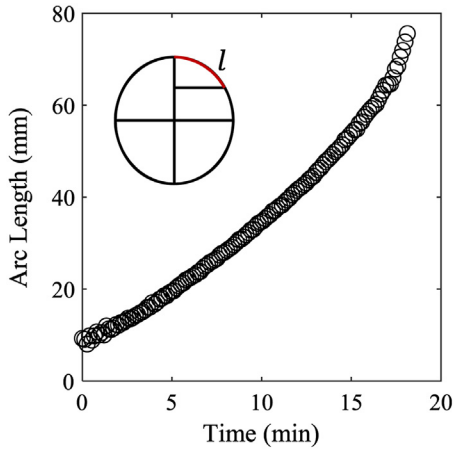

Fig. 3. An example of the time resolved arc length, l, for one of the 50 mm diameter trials.

4. Results

Video data from each experiment was processed to produce a time series for arc length, l. An example of time resolved arc length data is presented in Fig. 3. The arc length measurements can then be differentiated with respect to time to calculate the instantaneous flame spread rate as seen in Fig. 4.

The time resolved flame spread rates suggest that there is an unsteady incipient phase early after ignition, then the flame spread rates stabilize to a period of continual, gradual increase. The flame spread rate is observed to increase nearly linearly over the upper hemisphere of the sample. This stable period is then followed by a period of rapid acceleration in the flame spread rate once the flame front passes over the sample's equator.

These general trends in the flame spread rate behavior (e.g., steady period, rapid acceleration towards the end) were observed for both sphere diameters used in the experiments (see Fig. 5). The observed flame spread rates over the upper hemisphere were consistent, ranging from approximately 2.0–3.5 mm/min. Flame spread rates over the lower hemisphere were observed to exceed 15 mm/min for both diameters used. The variation

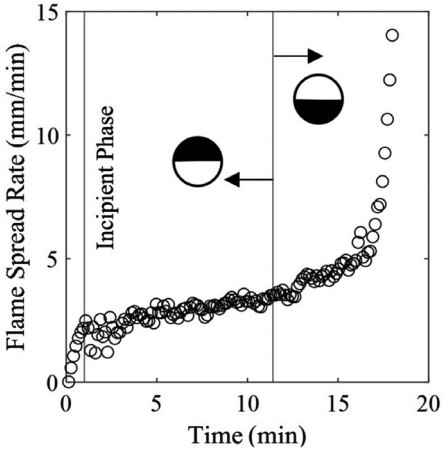

Fig. 4. The experimental flame spread rate calculated from the 50 mm diameter trial seen in Fig. 3. The incipient phase was observed prior to the first vertical line. The second vertical line indicates the flame spreading to the lower hemisphere.

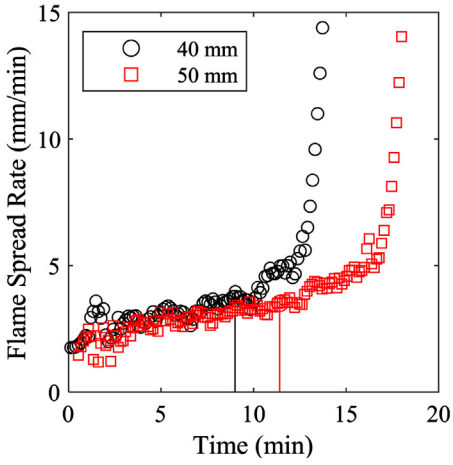

Fig. 5. Time resolved flame spread rates along the arc length for each of the diameter spheres tested. Vertical lines indicate the flame spreading to the lower hemisphere.

in the recorded flame spread rates between individual trials was on average less than 10% for the duration of the experiment (variation with respect to time ranged up to 30% when considering the rapid acceleration at the end of the experiment).

High speed video recordings were taken at four locations over the length of the sphere (taken at θ values of 60°, 90°, 120°, and 180°). The ambient flow velocity at each location was then approximated with the motion tracking algorithm described previously. Fig. 6 shows the approximate flow velocities at the flame front as a function of θ. The results suggest a distinct increase in the flow velocity as the flame spreads along the lower hemisphere. This increase in flow suggests that the

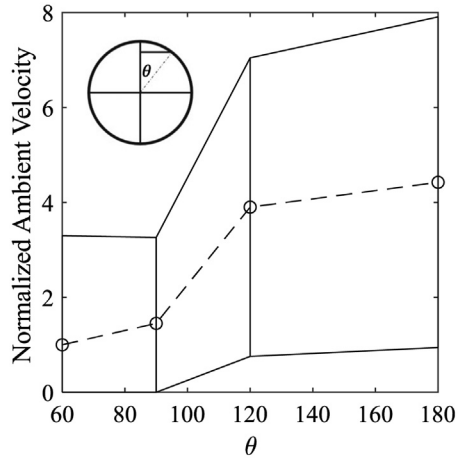

Fig. 6. The ambient flow velocity around the flame front as a function of $\boldsymbol{\theta}$. Velocities approximated using high speed footage and have been normalized relative to the location at 60° Error bars indicate $\pm 1\boldsymbol{\sigma}$ of the average value.

Stokes flow approximation used in Eq. (3) does not hold for the lower hemisphere.

Values presented in Fig. 6 have been normalized relative to the velocity taken at the first location ($\theta = 60°$) to indicate the relative increase in velocity as θ increases; the freestream velocity at $\theta = 60°$ was found to be approximately 0.4 m/s which is on the order of velocity predicted by $\sqrt{gD}$. The error bars in Fig. 6 are indicative of the relative variation in flow velocity at the flame front ($\pm 1\sigma$). The resolution and confidence of the analysis method lacks the fidelity to compare these measured values to the flow characterized by the Stokes flow solution for all values of θ. However, the analysis indicates that the velocities measured along the flame front on the lower hemisphere are higher than those observed for the upper hemisphere.

5. Analysis and discussion

The time resolved flame spread rate data presented in the previous section are indicative of two distinct flame spread regimes defined by spread above and below the sample equator (i.e., the upper and lower hemispheres). The following analysis sets out to describe the mechanisms that control the observed rates of flame spread and highlight the conditions that influence the different regimes of spread.

The flame spread rates in Fig. 5 indicate that while the general trends across spheres of different diameters are similar, the exact time resolved flame spread rates vary in time (i.e., different lengths of time to fully encircle each sphere). Eq. (3) suggests that the flame spread rate along the sphere can be characterized as a function of θ given the Stokes flow solution for u_θ. Fig. 7 presents the flame spread

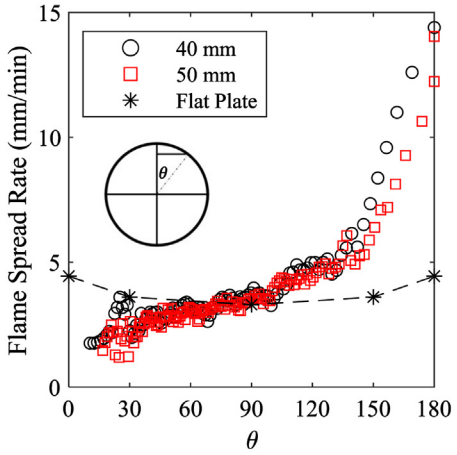

Fig. 7. Time resolved flame spread rates for each of the diameters tested plotted as a function of $\boldsymbol{\theta}$. Data also presented flame spread over flat plates at various inclinations taken from literature [14,15].

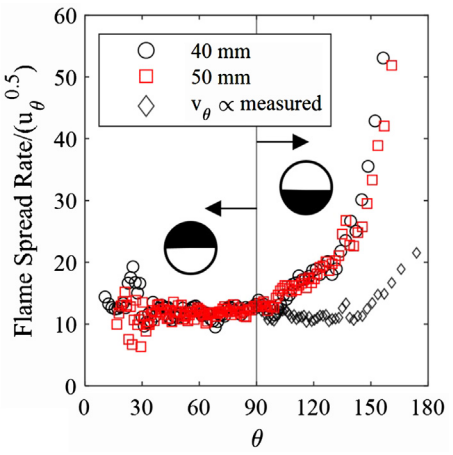

Fig. 8. Flame spread rate as a ratio to $\boldsymbol{u_\theta^{0.5}}$ for both the 40 mm and 50 mm spheres; the vertical line indicates the flame spreading to the lower hemisphere. Data also presented for the 40 mm sphere modified to account for the increased velocity along the lower hemisphere observed in Fig. 6.

rate for both the 40 mm and 50 mm spheres plotted as a function of θ, showing that the data between these two sphere sizes collapse.

The ability to normalize the flame spread rate behavior across both the 40 mm and 50 mm diameters suggest that the instantaneous flame spread rate for any normalized position is largely independent of diameter for the length scales tested, confirming the weak dependency on D as seen in Eq. (3).

Previous studies investigating flame spread rates over flat plates at various inclinations suggest that the opposed flow spread rate over PMMA plates should increase from $\theta = 0^\circ$ to $\theta = 90^\circ$ then decrease symmetrically as θ continues to 180° [14,15]. The transition between the spread regimes of the upper and lower hemisphere can also be seen to occur where $\theta = 90^\circ$. The observed flame spread over both hemispheres clearly deviates from the trend in flame spread rates over flat plates as a function of θ (with the exception of the intersection of the data where $\theta = 90^\circ$). The dissimilarity in the results for both hemispheres compared to flat plates suggests that orientation relative to the buoyant flow alone does not govern flame spread over the sphere. One must instead look at the flow conditions at the leading edge of the flame and employ Eq. (3) to characterize the observed flame spread. Thus, a spherical geometry offers the advantage of further investigating the connection between the ambient flow at the leading edge and the flame spread rate.

As suggested from Eq. (1), the flame spread rate is a function of the ambient flow conditions at the leading edge. Plotting the flame spread rate over a sphere scaled by $\sqrt{u_\theta}$ (Eq. (3)) results in a steady behavior for the upper hemisphere, as seen in Fig. 8. Additionally, Fig. 9 presents the flame spread rate over the upper hemisphere plotted against $\sqrt{u_\theta}$ to

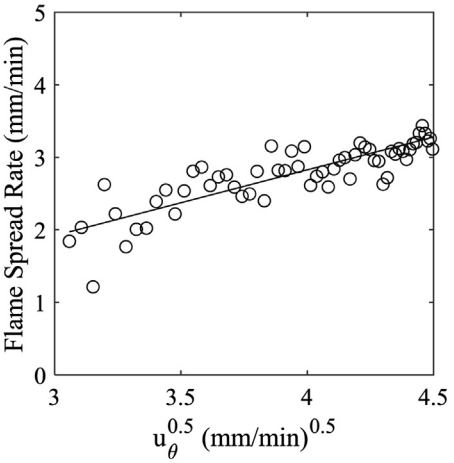

Fig. 9. The flame spread rate observed for the 50 mm sphere plotted against $u_\theta^{0.5}$ for the upper hemisphere (not including the incipient phase).

further support $v_f \propto \sqrt{u_\theta}$. This apparent proportionality between the flame spread rate and $\sqrt{u_\theta}$ suggests that the formulation of Eq. (3) is valid in describing the flame spread behavior over the upper hemisphere (i.e., the functionality of the Stokes flow solution adequately describes flow conditions for the upper hemisphere).

While utilizing u_θ has been shown to be useful in characterizing the upper hemisphere, Fig. 8 indicates that the flame spread rate over the lower hemisphere is not captured by the proportionality $v_f \propto \sqrt{u_\theta}$. Thus the Stokes flow relationship captured in u_θ is not an accurate representation of the lower hemisphere. Further insight into the flow

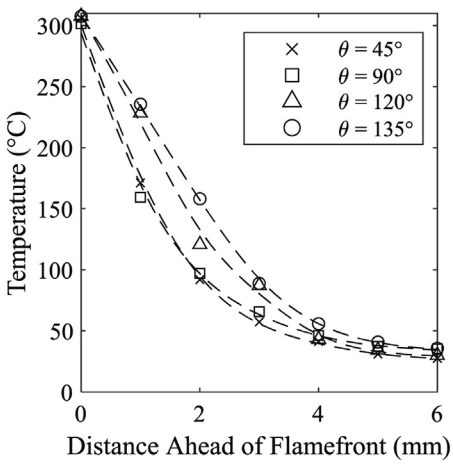

Fig. 10. Temperature measurements along the arc length ahead of the flame front taken at various values of θ.

characteristics along the length of the sphere can be determined through high speed recordings seen in Fig. 6. The high speed footage indicates that the ambient velocity at the leading edge increases as the flame passes over the equator to the lower hemisphere. The Stokes flow solution predicts that the flow rate around the sphere should decrease from the equator to the bottom of the sphere, and therefore the predictive ability of Eq. (3) breaks down when considering the lower hemisphere.

While Eq. (3) does not seem to describe the lower hemisphere as presented, the proportionality of $v_f \propto \sqrt{u_\theta}$ described in Eq. (1) appears to remain valid even after the flame front spreads to lower hemisphere. Fig. 6 illustrates an apparent increase in freestream velocity for θ greater than 90°. The freestream velocity at $\theta = 120°$ is approximated as 3.0 times greater than the velocity at $\theta = 90°$. This increase in flow and observed increase in flame spread rate corresponds to the functional behavior of Eq. (1); a threefold increase in u_θ suggests the flame spread rate at $\theta = 120°$ to be 1.7 times greater than at $\theta = 90°$. The linear proportionality of Eq. (1) therefore continues beyond 90° when considering the increased flow conditions along the lower hemisphere seen in Fig. 6 (see the modified data series in Fig. 8).

However, the rapid increase in flame spread rate beyond 150° does not appear to be caused by a commensurate increase in freestream velocity. This suggests that a different physical mechanism is causing this increase in flame spread rate. To investigate the physical origin of the acceleration in, temperature measurements were made at different locations within and on the surface of the sphere. Fig. 10 shows the measured surface temperature at various locations as the flame approaches. Measurements made on the upper hemisphere (45° and 90°) illustrate a consistent preheated region ahead of the flame front. Measured temperatures at locations on the lower hemisphere (120° and 135°) show higher temperatures ahead of the flame front. Further detail on temperature measurements throughout the sphere in-depth can be found in the Appendix.

Fig. 7 and Fig. 8 indicate that the rapid acceleration in flame spread rate occurs at a θ value between 150° and 160° for both diameters of spheres. This could be attributed to the preheating along the surface associated with interior heat transfer. The final acceleration in flame spread rate could also be attributed to the convergence of the preheated front ahead of the flame as the preheated regions meet at the bottom of the sphere. The remaining arc length from the flame front to the bottom of the sphere is 7–10 mm during the final observed acceleration. Fig. 10 suggests that the preheated region ahead of the flame front is of the same order (~5–7 mm). The final acceleration in flame spread rate is therefore a response to an absence of unheated material into which heat can be conducted away from the preheated region (i.e., an adiabatic condition).

Given the acceleration of the flame front occurs at the same value of θ for both diameters of sphere, the onset of this acceleration is likely independent of the remaining arc length. Interior heat transfer would therefore appear to contribute to the start of this acceleration over the lower hemisphere. Temperature measurments also suggest that the final acceleration is further enhanced due to the convergence of the preheated fronts at the bottom of the sphere.

6. Conclusions

Downward flame spread over PMMA spheres was classified into two distinct regimes of burning: spread over the upper hemisphere, and flame spread over the lower hemisphere. Instantaneous flame spread rates over the upper hemisphere were observed to increase nearly linearly as the flame front progressed down the upper hemisphere to the sample equator. Spread over the lower hemisphere, however, demonstrated rapidly accelerating instantaneous flame spread rates. For the entire duration of burning around the sphere, the flame spread rate was found to be unsteady (i.e., continuously increasing).

Flame spread over the upper hemisphere was characterized in this study using Eq. (3) derived from existing flame spread models adapted with a Stokes flow solution to characterize the flow conditions around the sphere (i.e., $v_f \propto \sqrt{u_\theta} \propto \sqrt{\sin\theta}$). Experimental results demonstrated that the model described in Eq. (3) accurately characterize flame spread over the upper hemisphere. Eq. (3) does not, however, adequately describe the velocity observed for the lower hemisphere (see Fig. 6).

Image processing techniques were used to indicate that the buoyancy induced flow at the flame front increased as the flame spread across the lower hemisphere. This increase in buoyant flow is consistent with the observed increase in flame spread rate for the lower hemisphere; however, the magnitude with which flame spread rate accelerates as the flame approaches the base of the sample suggests that the observed acceleration is not a result of this increased velocity alone. These results suggest that the rapid increase in flame spread rate at the end of each experiment is indicative of the merging of preheated fronts ahead of the flame at the bottom of the sphere and the onset of interior heat transfer becoming an increasingly significan mechanism of heat transfer.

This work establishes a theoretical basis and the fundamental mechanisms that govern opposed flame spread over spherical geometries. Additionally, an analytical model is presented to adapt existing flame spread theory to characterize flame spread over spheres (limited to the upper hemisphere). The novel definition of flame spread regimes over the two hemispheres of the sample provides a model through which a higher degree of characterization for flame spread over such geometries can be achieved. Furthermore this study identifies a distinct tranistion between two mechanisms of heat transfer, illustrating the increasing influence of interior heat transfer over the lower hemisphere.

Declaration of Competing Interest

The authors declare that they have no known competing financial interests or personal relationships that could have appeared to influence the work reported in this paper.

Acknowledgements

The authors would like to thank The University of Edinburgh's School of Engineering and the Rushbrook Foundation for their contributions in funding David Morrisset's PhD studies. Additionally the authors would like to thank Prof. Dougal Drysdale for his valuable contributions in conceptualizing this work.

Appendix

Fig. 11 illustrates the progression of the flame front over the duration of an experiment. The flame front is stable and allows for the front to be tracked using the video analysis techniques discussed previously in this work. The use of cast PMMA prevents

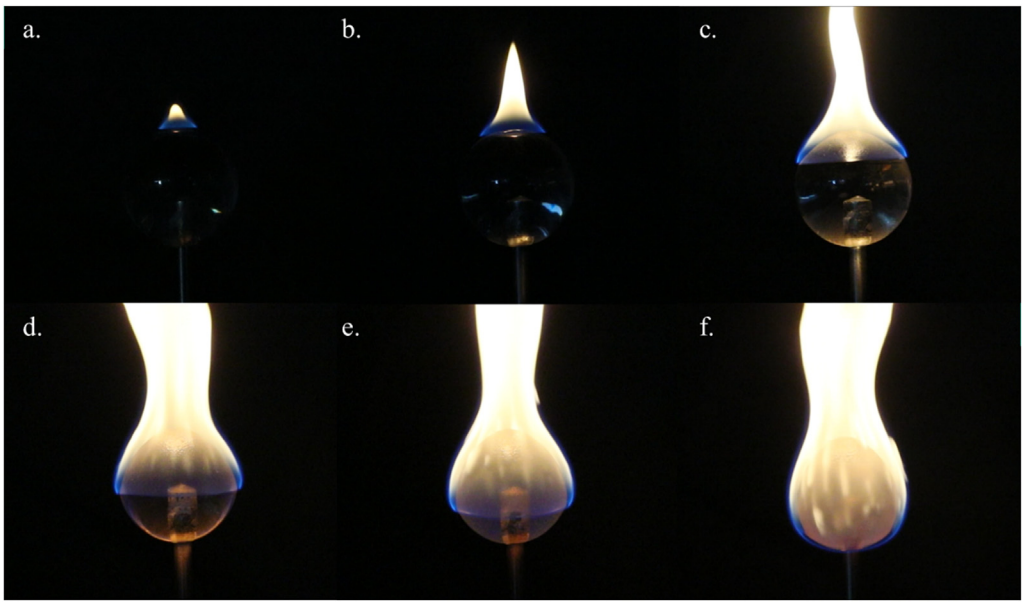

Fig. 11. A series of images showing the flame front progressing down the sphere at various times during an experiment: a) 90 s (once the ignition wire is removed), b) 3 min, c) 6:30 min, d) 10 min, e) 11:30 min, and f) 13:30 min.

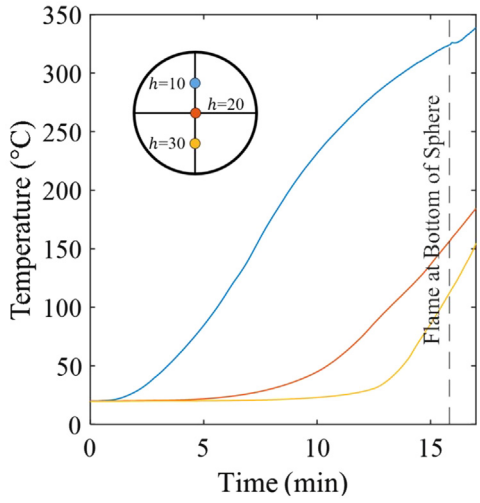

Fig. 12. In-depth temperature measurements at various depths along the centerline of a trial conducted with a 40 mm diameter sphere.

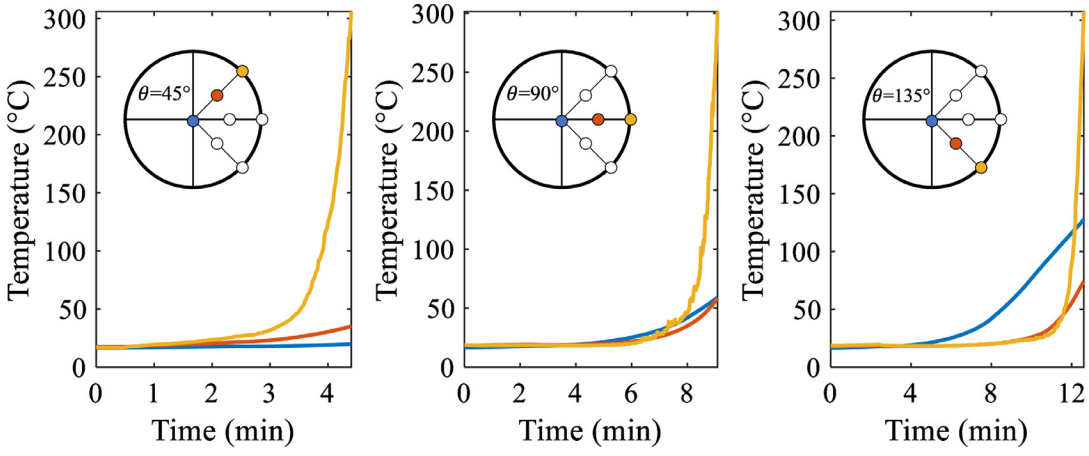

Fig. 13. Surface and in-depth temperature measurements recorded at various values θ of around the sphere.

the polymer from melting and dripping, as seen clearly in the images presented in Fig. 11.

Temperature measurements taken both at the surface and in-depth are presented in Figs. 12 and 13. Fig. 12 presents temperatures at various locations along the centerline of a 40 mm diameter sphere. The difference in time between the first two positions ($h = 10$ and $h = 20$) exceeding ambient temperature is observed to be much greater than the time between the two lower positions ($h = 20$ and $h = 30$) being heated above ambient. This is further evidence of the increasing relevance of interior heat transfer as the flame spreads along the lower hemisphere.

Fig. 13 shows temperature measurements taken radially from the center of the sphere at various values of θ. The radial temperature gradients illustrate that at 45° the temperatures consistently increase from the center to the surface. At 90°, the center temperature and the temperature at $r/2$ are nearly identical though nearly 250 °C lower than the surface temperature. At 135° the temperature at the center of the sphere exceeds that of the temperature at $r/2$.

References

[1] A.C. Fernandez-Pello, T. Hirano, Controlling mechanisms of flame spread, Combust. Sci. Technol. 32 (1–4) (1983) 1–31.
[2] I.S. Wichman, Theory of opposed-flow flame spread, Prog. Energy Combust. Sci. 18 (6) (1992) 553–593.
[3] Y. Hasemi, Surface flame spread, in: SFPE Handbook of Fire Protection Engineering, Springer, 2016, pp. 705–723.
[4] D. Drysdale, An Introduction To Fire Dynamics: Third Edition, 2011.

[5] J. Quintiere, Fundamentals of Fire Phenomena, Wiley, 2006.
[6] C. Fernandez-Pello, The Solid Phase, in: Combustion Fundamentals of Fire, 1995, pp. 31–100.
[7] J.N. De Ris, Spread of a laminar diffusion flame, Sympos. (Int.) Combust. 12 (1) (1969) 241–252.
[8] S.L. Olson, J.S. T'Ien, Buoyant low-stretch diffusion flames beneath cylindrical PMMA samples, Combust. Flame 121 (3) (2000) 439–452.
[9] C.T. Yang, J.S. T'ien, Numerical simulation of combustion and extinction of a solid cylinder in low-speed cross flow, J. Heat Transfer 120 (1998) 1055–1063.
[10] M. Endo, J.S. T'ien, P.V. Ferkul, S.L. Olson, M.C. Johnston, Flame growth around a spherical solid fuel in low speed forced flow in microgravity, Fire Technol 56 (1) (2020) 5–32.
[11] J.C. Yang, A. Hamins, M.K. Donnelly, Reduced gravity combustion of thermoplastic spheres, Combust. Flame 120 (1–2) (2000) 61–74.
[12] T. Delzeit, L. Carmignani, T. Matsuoka, S. Bhattacharjee, Influence of edge propagation on downward flame spread over three-dimensional PMMA samples, Proc. Combust. Inst. 37 (3) (2019) 3203–3209.
[13] E.J. Stalcup, J.S. T'ien, J. Jordan, Z. Wu, G. Nastac, C. Li, Upward flame spread and extinction over wavy solids, Combust. Sci. Technol. 192 (7) (2020) 1173–1198.
[14] A. Ito, T. Kashiwagi, Characterization of flame spread over PMMA using holographic interferometry sample orientation effects, Combust. Flame 71 (2) (1988) 189–204.
[15] A. Fernandez-Pello, F.A. Williams, Laminar flame spread over PMMA surfaces, Sympos. (Int.) Combust. 15 (1) (1975) 217–231.
[16] M. Lavid, A.L. Berlad, Gravitational effects on chemically reacting laminar boundary layer flows over a horizontal flat plate, Sympos. (Int.) Combust. 16 (1) (1977) 1557–1568.
[17] I.S. Wichman, Flame spread in an opposed flow with a linear velocity gradient, Combust. Flame 50 (1983) 287–304.
[18] H. Lamb, Hydrodynamics, University Press, 1924.
[19] P.J. Pritchard, J.W. Mitchell, Fox and McDonald's introduction to Fluid Mechanics, John Wiley & Sons, 2016.
[20] A. Acrivos, T.D. Taylor, Heat and mass transfer from single spheres in Stokes flow, Phys. Fluids 5 (4) (1962) 387–394.
[21] A.S. Rangwala, S.G. Buckley, J.L. Torero, Upward flame spread on a vertically oriented fuel surface: the effect of finite width, Proc. Combust. Inst. 31 (2) (2007) 2607–2615.